



## Studies of the hydrogen evolution reaction on Raney nickel–molybdenum electrodes

L. BIRRY and A. LASIA\*

Département de Chimie, Université de Sherbrooke, Sherbrooke, Québec, Canada J1K 2R1

(\* Author for correspondence, e-mail: a.lasia@usherbrooke.ca)

Received 7 August 2003; accepted in revised form 12 February 2004

**Key words:** doped Raney Ni electrodes, electrochemical impedance modeling, hydrogen evolution reaction, intrinsic activity

### Abstract

The hydrogen evolution reaction was studied in 1 M KOH at 25 °C on two types of electrodes: (i) pressed powders of Ni or NiMo with Al, heated at 700 °C; (ii) Ni–Al–Mo powders deposited by vacuum plasma spraying. These materials were treated with alkaline solution to leach out aluminum. Very active and stable Raney nickel–molybdenum electrodes were obtained from Al rich alloys. Adding molybdenum significantly improved catalytic activity. Electrochemical impedance spectroscopy was used to determine the apparent and intrinsic activities. Different ac models were tested and the appropriate one was selected. Intrinsic activities of these electrodes are smaller or equal to that of polycrystalline Ni and the origin of high apparent activities is related to the increase in real surface area.

### Introduction

Hydrogen produced by water electrolysis is a possible fuel of the future. It can be produced and used without pollution, avoiding use of fossil fuels. However, this method of hydrogen production remains costly. In order to increase electrode activity the real surface area and/or the intrinsic activity of the electrode material must be increased [1]. In our laboratory, many attempts have been made to develop efficient and stable electrode materials for the hydrogen evolution reaction (HER) in alkaline solution [1, 2]. Raney nickel is one of the most active and relatively inexpensive materials for this reaction [1, 2]. Raney nickel is produced by leaching aluminum or zinc from a precursor (Ni–Al or Ni–Zn) alloy with caustic solution, leaving a very porous material. This increases its real surface area and leads to lower overpotentials. Various techniques of preparation of these materials have been used:

- electrocodeposition of Raney Ni powder with Ni [3–5],
- electrodeposition of Ni–Zn alloys [6],
- plasma spraying [7–10],
- rolling of Al and Ni foils followed by heat treatment [8, 11],
- pressing and heating Ni + Al powders [12, 13],
- pressing Raney Ni with fractal Ni powder [13],
- sintering Raney Ni [14], etc.

For electrodes prepared by pressing Ni and Al powders a dramatic increase in activity was found after heating them above the Al melting point (660 °C), which is connected with the formation of intermetallic Ni–Al phases [12]. This is a simple method of preparation of very active electrodes, however, leached Ni–Al electrodes are not very stable during long term polarization. Tanaka et al. [15] showed importance of the nature of Ni–Al phases on the catalytic activity. The most active electrodes were obtained from Al rich alloys (NiAl<sub>3</sub>) from which Al is very easily leached out but they were the least stable. It was also found [7, 10, 16–18] that adding molybdenum to Raney nickel improves its catalytic activity. Ni–Mo alloys are considered as good catalysts for the HER although other studies have not confirmed these findings [1].

In the present work, active Ni–Al and Ni–Al–Mo alloys were prepared by two techniques:

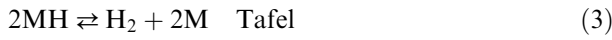
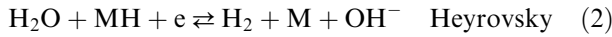
- by pressing and heating Ni and Al or Ni–Mo and Al powders, at 700 °C,
- by vacuum plasma spraying.

The structure and composition were studied using scanning electron microscopy (SEM), X-ray diffraction (XRD), and elemental microanalysis including mapping (EDX). The mechanism and kinetics of the HER on these electrode materials were studied using steady-state polarization and electrochemical impedance

spectroscopy (EIS). Several models describing the impedance data were tested and the appropriate model was selected.

## 2. Theory

The HER in alkaline solutions proceeds through three following steps:



where M represents metal on the electrode surface and MH hydrogen adsorbed on the electrode surface. For the Volmer–Heyrovsky mechanism (i.e., neglecting the Tafel reaction) and assuming that  $\beta_1 = \beta_2 = \beta$ , where  $\beta_1$  and  $\beta_2$  are the symmetry coefficient of the steps 1 and 2, the following relation between the current density,  $j$ , and overpotential,  $\eta$ , may be given [19]:

$$j = \frac{2Fk_1k_2e^{-\beta f\eta}(1 - e^{2f\eta})}{(k_1 + k_2) + (k_{-1} + k_{-2})e^{f\eta}} \quad (4)$$

where  $k_{\pm 1}$ ,  $k_{\pm 2}$  are the forward (+) and backward (−) rate constants and  $f = F/RT$ . At high overpotentials this expression becomes:

$$j = 2F \frac{k_1k_2}{k_1 + k_2} e^{-\beta f\eta} \quad (5)$$

which indicates that the current density is directly proportional to the harmonic mean of the forward rate constants. Conway and Harrington [20] presented a theory of the faradaic impedance for the HER [21]. The faradaic impedance is given by the following expression:

$$\frac{1}{Z_f} = A + \frac{B}{j\omega + C} \quad (6)$$

where

$$A = \frac{1}{R_{ct}} = -F \left( \frac{\partial r_0}{\partial \eta} \right)_\theta \quad (7)$$

$$B = -\frac{F^2}{\sigma_1} \left( \frac{\partial r_0}{\partial \theta} \right)_\eta \left( \frac{\partial r_1}{\partial \eta} \right)_\theta \quad (8)$$

$$C = -\frac{F}{\sigma_1} \left( \frac{\partial r_1}{\partial \theta} \right)_\eta \quad (9)$$

$r_0 = v_1 + v_2$ ,  $r_1 = v_1 - v_2 - 2v_3$ ,  $v_1, v_2, v_3$  are the rates of Volmer, Heyrovsky, and Tafel reactions, respectively,  $\theta$  is the surface coverage by adsorbed hydrogen and  $\sigma_1$  is the charge necessary for a monolayer coverage by adsorbed hydrogen. The parameter  $A$  represents the inverse of the charge transfer resistance  $R_{ct}$  and for  $\beta_1 = \beta_2 = \beta$  may be expressed as:

$$A = \frac{1}{R_{ct}} = \frac{F^2}{RT} e^{-\beta f\eta} \left[ \frac{(k_1k_{-1} + k_2k_{-2})e^{f\eta} + k_1k_2(2\beta + e^{2f\eta})}{k_1 + k_2 + (k_{-1} + k_{-2})e^{f\eta}} \right] \quad (10)$$

which, for  $\beta = 0.5$ , reduces to a known form [2, 22]. At negative overpotentials this expression becomes:

$$A = \frac{1}{R_{ct}} = \frac{2\beta F^2}{RT} \left( \frac{k_1k_2}{k_1 + k_2} \right) e^{-\beta f\eta} \quad (11)$$

and it is proportional to the harmonic mean of  $k_1$  and  $k_2$ . Comparison of (5) and (11) shows that these two parameters are proportional to each other.

Total electrical equivalent model of the HER on metal electrodes consists of the solution resistance  $R_s$  in series with a parallel connection of the double layer capacitance  $C_{dl}$  and the faradaic impedance  $Z_f$ . This model predicts formation of two semicircles on the complex plane plots; the first arises from coupling of the charge transfer resistance and double layer capacitance,  $R_{ct} - C_{dl}$  and the second from coupling of the two kinetic parameters  $R_p - C_p$ , related to the parameters  $R_{ct}$ ,  $B$ , and  $C$ . The faradaic impedance equals:

$$Z_f = R_{ct} + \frac{1}{j\omega C_p + \frac{1}{R_p}} \quad (12)$$

where

$$R_p = -\frac{1}{\frac{A^2 C}{B} + A} \quad (13)$$

and

$$C_p = -\frac{A^2}{B} \quad (14)$$

However, when  $A \gg B/(j\omega + C)$  only one semicircle is observed.

For solid electrodes, the double layer capacitance  $C_{dl}$  is substituted by a constant phase element (CPE). Its impedance is given by [23]:

$$Z_{CPE} = \frac{1}{T(j\omega)^\phi} \quad (15)$$

where parameter  $\phi$  is related to the constant phase angle  $\alpha = 90^\circ(1 - \phi)$  and  $T$  is a capacity parameter in

$F \text{ cm}^{-2} \text{ s}^{\phi-1}$ , related to the double layer capacitance [23]:

$$T = C_{\text{dl}}^{\phi} (R_s^{-1} + A)^{1-\phi} \quad (16)$$

The presence of the CPE was initially attributed to the surface roughness or porosity (geometric factors) [21], however, it was found experimentally that these factors were unrelated [24]. Recent studies attribute it to the atomic scale inhomogeneities, see [21, 25] and references therein. It is well known that adding small amount of adsorbing ions causes immediate appearance of the CPE [26].

Two models have been used to explain the impedance of Ni–Al and Ni–Al–Mo electrodes. The first is the so called 1CPE model shown in Figure 1(a) and Table 1 [2, 12–14, 19, 27]. In general, it can produce one or two semicircles on the complex plane plots. The second model is the two CPE model introduced by Chen and Lasia [28], see Figure 1(b) and Table 1. It can also produce two semicircles but the first one, potential independent, is related to the surface porosity and the second, potential dependent, is related to the HER.

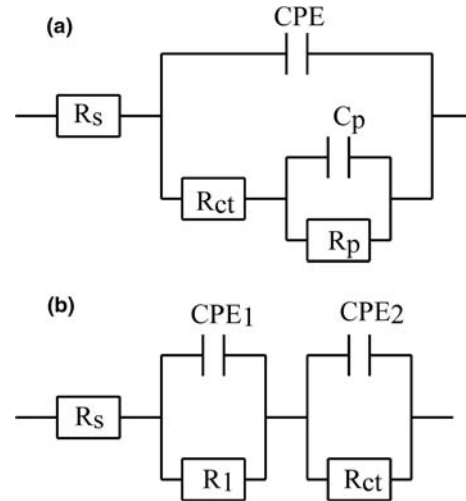
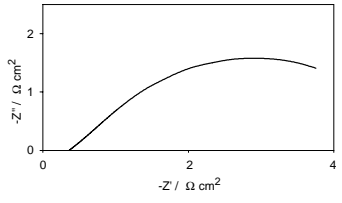
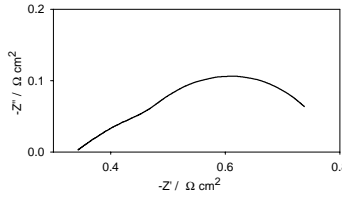
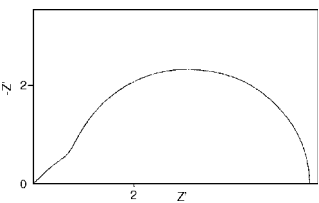


Fig. 1. Equivalent circuits used for the HER. (a) 1CPE model, (b) two CPE model.

For deep cylindrical pores on the electrode surface, de Levie [29] proposed a porous electrode model. The total impedance is expressed as:

Table 1. Equivalent models

Model	Nyquist plots	Total impedance	Obtained parameters	Calculated parameters
1CPE	One or two semicircles, both potential dependent	$Z_T = R_s + Z_f$ where $Z_f$ is given by the Equation 6	$A, B, C, R_s, T, \phi$	$R_{\text{ct}} = 1/A$ $R_p = \frac{R_{\text{ct}}^2  B }{C - R_{\text{ct}}  B }$ $T = C_{\text{dl}}^{\phi} (R_s^{-1} + A)^{1-\phi}$
2CPE	Two semicircles: first: potential independent, second: potential dependent	$\frac{1}{Z_f} = A + \frac{B}{j\omega + C}$	$A_1, A_2, R_s,$ $T_1, \phi_1, T_2, \phi_2$	$R_{\text{ct}} = 1/A_2$ $T_2 = C_{\text{dl}}^{\phi_2} (R_s^{-1} + A_2)^{1-\phi_2}$
Semi-infinite porous model (1CPE)	 OR 	$Z_T = R_s + R_{\Omega,p} a^{1/2} [1/Z_f + (j\omega)^{\phi} T]^{-1/2}$	$A/u, B/u, C, R_s,$ $T/u, \phi$ with $u = R_{\Omega,p}^2 a$	$uR_{\text{ct}}, C_{\text{dl}}/u, C_{\text{dl}} \sim \text{real surface area}$  $1/R_{\text{ct}} \sim k$ intrinsic activity: $\sim 1/(R_{\text{ct}} C_{\text{dl}})$
Finite length porous model	2 semicircles potential dependent 	$Z = R_s + (R_{\Omega,p}/\Lambda^{1/2}) \coth(\Lambda^{1/2})$  $Z_f$ in $\Lambda$ is given by Equation 6	$A_p, B_p, \phi,$ $R_s, R_{\Omega,p}$	$A_p = aR_{\text{ct}}$ $B_p = T/a$ $R_{\text{ct}} = R_{\Omega,p} A_p$ $T = B_p/R_{\Omega,p}$

$$Z = R_s + (R_{\Omega,p}/\Lambda^{1/2}) \coth(\Lambda^{1/2}) \quad (17)$$

where  $R_{\Omega,p} = \rho l/n\pi r^2$  and  $\Lambda = (2\rho l^2/r)(1/Z_f + j\omega C_{dl})$ . In the case of the HER, the faradaic impedance is given by Equation 6, although, in practice, one semicircle is observed on the complex plane plots because  $Z_f = R_{ct}$  [2, 27, 30]. This model predicts a straight line at 45° at high frequencies, followed by one or two deformed semicircles (Figure 2(a)) in these plots. For real electrodes the double layer capacitance is replaced by the CPE [30]. Equation 17 has two limiting cases depending on the penetration depth of the ac signal in the pores,  $\lambda = (rZ_0/2\rho)^{1/2}$ , where  $Z_0 = (1/Z_f + j\omega C_{dl})^{-1}$ :

(a) For  $l \ll \lambda$ ,  $\Lambda^{1/2} = l/\lambda \rightarrow 0$ ,  $\coth \Lambda^{1/2} \rightarrow \Lambda^{-1/2}$  and

$$Z = R_s + R_{\Omega,p}/\Lambda = R_s + (1/s) \left[ 1/Z_f + (j\omega)^\phi T \right]^{-1} \quad (18)$$

where  $s = 2n\pi r l$  is the total surface area of the pore walls. In this case, the signal penetrates up to the bottom of the pore, the electrode behaves as a flat one, and the complex plane plots may be described by a simple CPE model (Figure 2(b)).

(b) For  $l \gg \lambda$ , the pores behave as infinitely deep, the signal cannot penetrate up to the bottom of the pores,  $\Lambda \rightarrow \infty$ ,  $\coth \Lambda^{1/2} \rightarrow 1$ , and the equation 17 simplifies to:

$$Z = R_s + R_{\Omega,p}/\Lambda^{1/2} = R_s + R_{\Omega,p} a^{1/2} \left[ 1/Z_f + (j\omega)^\phi T \right]^{-1/2} \quad (19)$$

As a result, the complex plane plot is a deformed semicircle (Figure 2(c)). In the case when the faradaic impedance is described by Equation 6, one can only obtain parameter  $uZ_f$

$$uZ_f = \frac{1}{\frac{1}{uR_{ct}} + \frac{B/ua}{j\omega + C}} = (uR_{ct}) + \frac{1}{\frac{1}{(uR_p)} + j\omega \left( \frac{C_p}{u} \right)} \quad (20)$$

where  $u = R_{\Omega,p}^2 a = \rho/(n\pi)^2 (2r^3)$ , from which three parameters:  $uR_{ct}$ ,  $uR_p$  and  $C_p/u$  may be found, however,  $R_{ct}$ ,  $R_p$  and  $C_p$  cannot be determined independently. All the models used for our electrode materials are described in Table 1. In the latter case, in order to

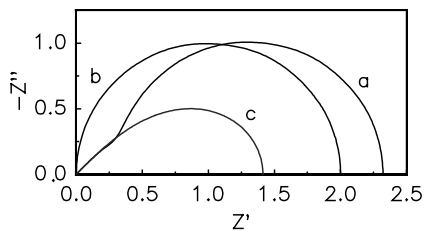


Fig. 2. Complex plane plots on porous electrode: (a) general, Equation 17, (b) shallow pores, Equation 18, (c) semi-infinite pores, Equation 19.

compare the specific activities of different electrodes, one can evaluate:

$$(uR_{ct})(C_{dl}/u) = R_{ct}C_{dl} = \left( \frac{R_{ct}^0}{s} \right) (C_{dl}^0 s) = R_{ct}^0 C_{dl}^0 \quad (21)$$

where  $R_{ct}^0$  and  $C_{dl}^0$  are specific (per unit of the real surface area) charge transfer resistance and double layer capacitance. This parameter gives the product of the specific charge transfer resistance, related to the electrode kinetics, and a specific double layer capacitance, which is similar for all metallic surfaces. Therefore, the product of the experimentally accessible parameters  $(uR_{ct})(C_{dl}/u)$  or  $(uR_{ct})(T/u)$  is a direct measure of  $R_{ct}^0$  and  $1/[(uR_{ct})(C_{dl}/u)]$  is proportional to the electrode specific activity.

### 3. Experimental

#### 3.1. Electrode preparation

Ni–Al powder electrodes were prepared from Inco Ni type 255 and Al (Anachemia AC-353) powders. Ni–Al–Mo alloys were prepared from Ni–Mo precursor alloys and aluminum powders. The following precursor alloys were used:

- 87.5 wt.% Ni, 12.5 wt.% Mo (Consolidated Astro-nautics, 99%, 45  $\mu\text{m}$ ),
- 84 wt.% Ni, 16 wt.% Mo (Goodfellow, 99%, 45  $\mu\text{m}$ ),
- 80 wt.% Ni, 20 wt.% Mo (Goodfellow, 99%, 150  $\mu\text{m}$ ),
- 70 wt.% Ni (Inco 255), 30 wt.% Mo (10  $\mu\text{m}$ ) prepared by vacuum plasma spraying (CRTP, Université de Sherbrooke).

After mixing, powders were pressed, then heated at 700 °C for 12 h under nitrogen atmosphere. The formation of Ni–Al intermetallic compounds was confirmed by the XRD analysis. These electrodes were attached to a copper cylinder with a silver epoxy and fitted in a shrinkable tube, exposing a geometric area of 0.5 cm<sup>2</sup>. To dissolve the aluminum, the electrodes were leached in a 30% KOH solution (BDH, 85%) containing 10% of K–Na tartrate, at 70 °C for 24 h.

Plasma spraying was also used to prepare Ni–Al–Mo electrode materials. The electrode materials were prepared at CRTP (Plasma Technology Research Center) of the University of Sherbrooke by Glen Lemoine and Jerzy Jurewicz. The precursor alloys were prepared by high impact ball milling of powders followed by alloying using self-propagation high-temperature synthesis (SHS) and then deposited by vacuum HF plasma spraying. Alloys having the following stoichiometry were prepared: NiAl<sub>5</sub>Mo<sub>2</sub> (T), NiAl<sub>8</sub>Mo (G), NiAl<sub>7.5</sub>Mo<sub>1.5</sub> (H), NiAl<sub>5</sub>Mo<sub>0.67</sub> (I), 46%NiAl<sub>3</sub> + 54%Ni<sub>2</sub>Al<sub>3</sub> (B) and the mixtures 25–75% of T + B. The obtained electrode materials were leached in the same way as the alloyed powder electrodes.

### 3.2. Electrochemical measurements

A two compartment Pyrex glass cell separated by a Nafion membrane (Dupont de Nemours 450) was used to carry out the electrochemical measurements. A nickel foil was used as the counter electrode. Electrochemical tests were made in 1 M KOH solution (Aldrich, 99%) containing  $10 \text{ g l}^{-1}$  of ethylenediamine tetraacetic acid (EDTA) (Fisher) [31] at 25 and 70 °C. Solutions were bubbled with  $\text{N}_2$  before measurements. The Hg/HgO/1 M KOH reference electrode was connected to the cell through a Luggin capillary. KCN (Fisher) was added to some solutions as a distinction criterion between the equivalent circuits.

Tafel curves were registered galvanostatically in the current range of 300 mA to 0.01  $\mu\text{A}$  using EG&G PAR system (model 273). At higher current densities, current interruption technique was used [14]. The kinetic parameters (i.e., Tafel slope  $b$ , exchange current density  $j_0$  and overpotential at the current density of  $250 \text{ mA cm}^{-2}$ ,  $\eta_{250}$ ) were obtained after correction for the ohmic drop. Ac impedance measurements were performed in the frequency range of 10 kHz to 8 mHz using a frequency response analyzer (FRA) Solartron model 1260 and a potentiostat Solartron model SI 1287. The ac amplitude was 10 mV peak to peak. The approximations of the impedance results were made for various models (Tables 1 and Figure 1(a) and (b)) using modified complex non-linear least-squares fitting program (CNLS) [32].

## 4. Results

### 4.1. Pressed and heated Ni–Al–Mo powders

**4.1.1. Composition and surface morphology of electrodes**  
Heating of Ni or Ni–Mo and Al powders produced intermetallic phases. XRD of  $\text{Ni}_2\text{Al}_3$  shows practically pure phase, but that of  $\text{NiAl}_3$  shows also small amount of  $\text{Ni}_2\text{Al}_3$ . The diffractogram of the sample having global stoichiometry of  $\text{Ni}_2\text{Al}_5$  shows mainly  $\text{Ni}_2\text{Al}_3$  and  $\text{NiAl}_3$ . Figure 3 shows XRD diffractograms of Ni–Al–Mo samples. Diffractogram of  $\text{Ni}_2\text{Al}_3\text{Mo}_{0.175}$  shows presence of  $\text{Ni}_2\text{Al}_3$  and  $\text{NiAl}_5\text{Mo}_2$ ,  $\text{Ni}_2\text{Al}_5\text{Mo}_{0.175}$  the presence of  $\text{NiAl}_3$  and  $\text{Ni}_2\text{Al}_3$ , and  $\text{NiAl}_3\text{Mo}_{0.0875}$  the presence of  $\text{NiAl}_3$ ,  $\text{Ni}_2\text{Al}_3$  and  $\text{NiAl}_5\text{Mo}_2$ . Leaching produces very broad Ni peaks, indicating nanostructured surface layer, Figure 4, similarly to those presented in Refs. [12, 14, 15]. EDX analysis of the samples presented in Figure 5 shows that after leaching process Ni peaks increased considerably and aluminum content decreased, but Al is still present in the sample after leaching. Moreover, Mo peaks are visible on both spectra. Peaks of potassium visible after leaching arise from the leaching solution. These findings were confirmed by mapping of Ni, Al and Mo before and after leaching.

Figure 6 shows the morphological changes of the electrode surface during leaching process. Grain boundaries are dissolved more easily and there is a formation of submicrometric pores on the surface. Crosssection view of the leached electrode, Figure 7, shows that leaching takes place up to  $\sim 1.5 \text{ mm}$ . EDX analysis of this electrode shows that Al is always present in the leached electrode, but the ratio Mo/Ni decreases during leaching, which indicates that Mo is also partially removed during this process.

It was also found that adding molybdenum improves mechanical and long-term stability of the obtained materials. The electrodes were studied in KOH solution for several (3–4) days and their catalytic activities did not change during this period, similarly to the results observed in the literature for other Mo-doped Raney nickel electrodes [17, 33]. On the other hand, Ni–Al electrodes were more fragile and after few days broke up, in particular  $\text{NiAl}_3$  which was the most porous one.

### 4.1.2. Steady-state polarization curves

The apparent activity of the electrodes was studied in 1 M KOH by recording steady-state polarization curves. From the linear part of the Tafel curves, kinetic parameters were determined and they are presented in Table 2. An example of the Tafel curve obtained on  $\text{NiAl}_3\text{Mo}_{0.175}$  electrode is presented in Figure 8. In general, the electrode activities increase with increase in Al and Mo content. For the electrodes characterized by stoichiometry  $\text{Ni}_2\text{Al}_3$  the Tafel slopes,  $b$ , are large, from  $-200 \text{ mV dec}^{-1}$  for  $\text{Ni}_2\text{Al}_3$  to  $-150 \text{ mV dec}^{-1}$  for  $\text{Ni}_2\text{Al}_3\text{Mo}_{0.306}$ . They are smaller for  $\text{Ni}_2\text{Al}_5$ , from  $-157$  to  $-119 \text{ mV dec}^{-1}$ , and decrease with increase in Mo content. The smallest Tafel slopes were obtained for the electrodes having stoichiometry of  $\text{NiAl}_5$ . In general, the Tafel slopes decrease with increase in temperature, which indicates that the apparent transfer coefficient is increasing with temperature as  $b = RT \ln 10 / \alpha F$ . High Tafel slopes were also observed earlier at sintered [14] and metallurgically prepared [13] Raney Ni electrodes.

The practical measure of the electrode activity is overpotential at a given current density, in our studies at  $250 \text{ mA cm}^{-2}$ ,  $\eta_{250}$ . Electrodes having stoichiometry  $\text{Ni}_2\text{Al}_3$  are characterized by the smallest activity with  $\eta_{250} = -280 \text{ mV}$ . The activity increased after doping with Mo,  $\eta_{250} = -160 \text{ mV}$  for atomic fraction of Mo of 0.175 and 0.233. It increased further after increase of the Mo content, for  $\text{Ni}_2\text{Al}_3\text{Mo}_{0.306}$   $\eta_{250} = -70 \text{ mV}$ . Electrodes based on the stoichiometry  $\text{Ni}_2\text{Al}_5$  are more active with than without Mo; the activity of  $\text{Ni}_2\text{Al}_5$  is  $\eta_{250} = -253 \text{ mV}$  and those containing Mo are characterized by  $\eta_{250}$  between  $-60$  and  $-70 \text{ mV}$ . Finally, the most active electrodes are those containing the highest amount of Al, for  $\text{NiAl}_3$   $\eta_{250} = -136 \text{ mV}$  decreasing to  $-57 \text{ mV}$  for  $\text{NiAl}_3\text{Mo}_{0.306}$ . Electrode activities increase with increase in the temperature. The highest activity of  $-33 \text{ mV}$  was obtained for  $\text{NiAl}_3\text{Mo}_{0.306}$  at 70 °C.

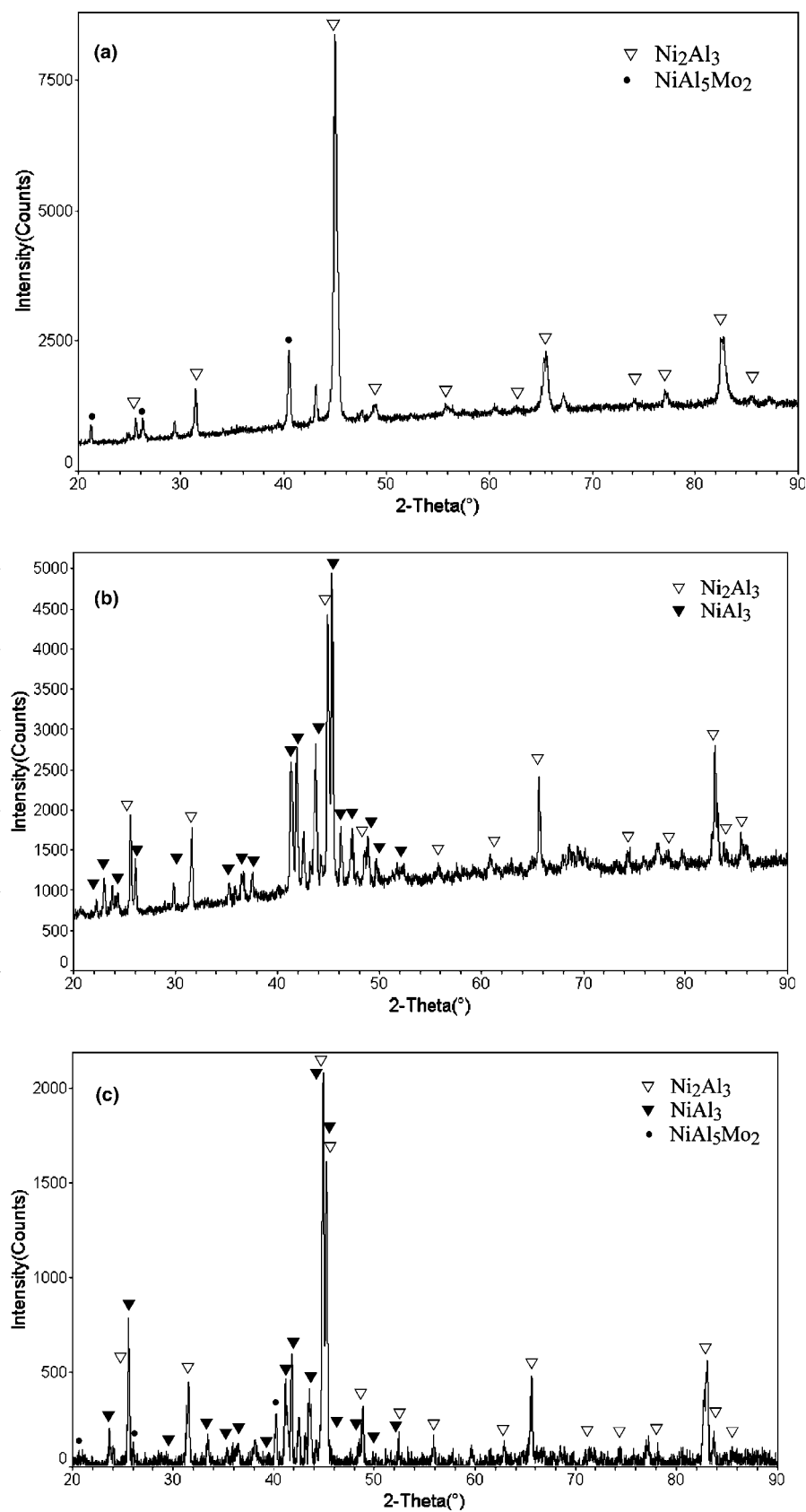


Fig. 3. XRD spectra of: (a)  $\text{Ni}_2\text{Al}_3\text{Mo}_{0.175}$ , (b)  $\text{Ni}_2\text{Al}_3\text{Mo}_{0.175}$  and (c)  $\text{NiAl}_3\text{Mo}_{0.0875}$ .

The HER reaction was also studied in the presence of poison KCN. Figure 8 shows an example of the Tafel curves for the HER in the absence and in the presence of

$\text{CN}^-$ . Cyanides poison the electrode, increase the Tafel slope and decrease the activity towards the HER:  $\eta_{250}$  increases from  $-71$  to  $-110$  mV.

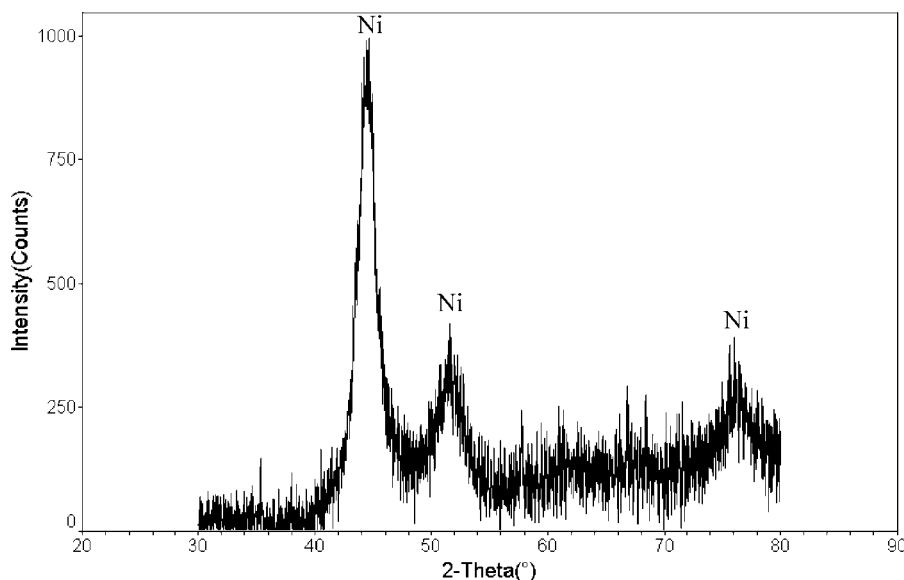


Fig. 4. XRD spectrum of the electrode  $\text{Ni}_2\text{Al}_5\text{Mo}_{0.175}$  after leaching in KOH for 24 h at 70 °C; see text for details.

#### 4.1.3. Impedance spectroscopy

Activity of the electrodes was also studied using electrochemical impedance spectroscopy. Examples of the complex plane plots obtained for Ni–Al and Ni–Al–Mo electrodes are shown in Figures 9 and 10. Two types of spectra were obtained: the first containing one deformed semicircle and the second containing two semicircles. Electrodes without Mo and those composed of  $\text{Ni}_2\text{Al}_3$  and containing up to 0.233 of Mo displayed one semicircle while other electrodes displayed two semicircles.

The electrodes displaying one semicircle could be modeled using (a) 1CPE or (b) semi-infinite porous model with  $Z_f = R_{ct}$ ; the finite length porous model may be rejected as it produces straight line at 45° at high frequencies, followed by a distinguished semicircle, see Figure 2(a). The experimental impedance data were fitted using these two models. 1CPE model gives unusually low values of the parameter  $\phi$ , between 0.48 and 0.66, and extremely large values of the double layer capacitance, between 0.3 and 6.8  $\text{F cm}^{-2}$  of the geometric surface area. Use of semi-infinite porous model gives the constant phase angle between 0.81 and 1. It should be noticed that at high frequencies a straight line at  $\sim 45^\circ$  is observed on the complex plane plots, which suggests the semi-infinite porous model. Comparison of these two models using test F showed that the fit to the semi-infinite porous model is statistically much better. However, using this model it is impossible to extract  $R_{ct}$  and  $C_{dl}$  from the experimental data.

The two semicircles observed for NiAlMo electrodes might be related to the kinetics of the HER, Equation 6, or the high frequency (HF) semicircle related to the porosity and the low frequency (LF) one to the kinetics of the HER (two CPE model). In our earlier works [28, 31] we have developed several criteria to distinguish between these two possibilities. The first one is to check

the dependence of the radius of both semicircles as a function of overpotential; only the kinetics of the electrocatalytic reactions depends on overpotential. However, the overpotential range used for these measurements is too small to determine the kinetic dependence of the HF semicircle, because the activity of the electrodes is very high and above  $\eta = -40$  mV, the HER is so vigorous that hydrogen bubbles cause too much interference and good impedance spectra cannot be obtained.

The effect of temperature is another criterion; the kinetics of electrocatalytic reactions is more sensitive to changes in the temperature than the solution resistance. The influence of temperature (25–70 °C) on the complex plane plots obtained at  $\text{NiAl}_3\text{Mo}_{0.262}$  electrode at  $\eta = -14$  mV is shown in Figure 11. The diameters of both semicircles decrease with the increase in temperature indicating that they are both related to the electrode kinetics.

The effect of poison can also be used to verify the nature of the semicircles. In the next experiment  $5 \times 10^{-2}$  M KCN was added to the solution. Tafel curves shown in Figure 8 revealed a decrease in the electrode kinetics. Figure 12, and the diameter of both semicircles increased. This effect is also illustrated in Figure 13 where the diameters of both semicircles are plotted as functions of overpotential in the absence and presence of the poisons. The analysis presented above confirms that both semicircles are related to the electrode kinetics. This indicates that two models may approximate the experimental complex plane plots: (a) 1CPE or (b) semi-infinite porous models, both with Equation 6 for the faradaic impedance of the HER. Complex nonlinear least-squares approximations were carried out for these two models. The test F could not distinguish between these two models, they both gave the same goodness of fit.

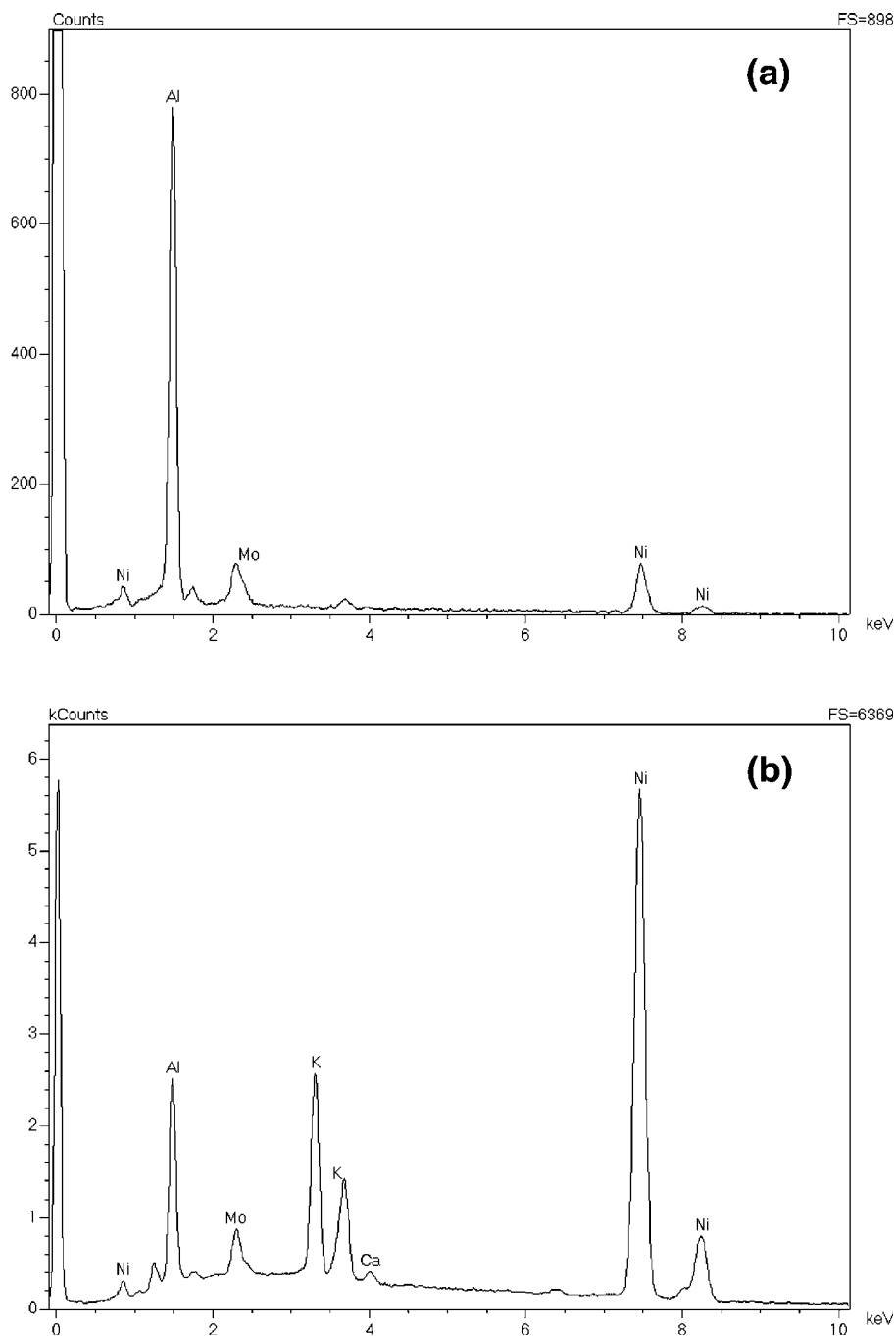


Fig. 5. EDX analysis of  $\text{Ni}_2\text{Al}_5\text{Mo}_{0.175}$ : (a) before and (b) after leaching.

However, approximation by the ICPE model gave very low values of the parameter  $\phi \sim 0.6$  and unusually large values of the double layer capacitance, up to  $6.8 \text{ F cm}^{-2}$ . On the other hand, using a semi-infinite porous model these values are close to 1. Therefore, the latter model was used for all the approximations for NiAl and NiAlMo electrodes. The results of approximations obtained at the same overpotential  $\eta = -35 \text{ mV}$  are shown in Table 3. The intrinsic activities (per unit of the real surface area, Equation 21) of our electrodes are displayed in the last column as  $1/(R_{ct}T)$ , which is proportional to the rate constants of the HER according to Equations 10 and 11, and

represents a comparative measure of this activity. For comparison the same parameter was estimated for polycrystalline Ni electrode in the same conditions. From Ref. [19],  $\log(R_{ct}^0/\Omega \text{ cm}^2) = -4.2$  and  $C_{dl}^0 = 42 \mu\text{F cm}^{-2}$ , which gives  $1/(R_{ct}^0 C_{dl}^0) = 1.5 \text{ s}^{-1}$ . Between the materials studied the lowest activities were found for electrodes based on  $\text{Ni}_2\text{Al}_3$  and  $\text{Ni}_2\text{Al}_5$  ( $-0.005 \text{ s}^{-1}$ ), followed by that of  $\text{NiAl}_3$  ( $0.02 \text{ s}^{-1}$ ). These activities are much lower than that observed for polycrystalline Ni. Addition of Mo increases the activity, which, in some cases, attains that of polycrystalline Ni. In general, activity increases with increase in the Mo content in the precursor alloy. Because for some



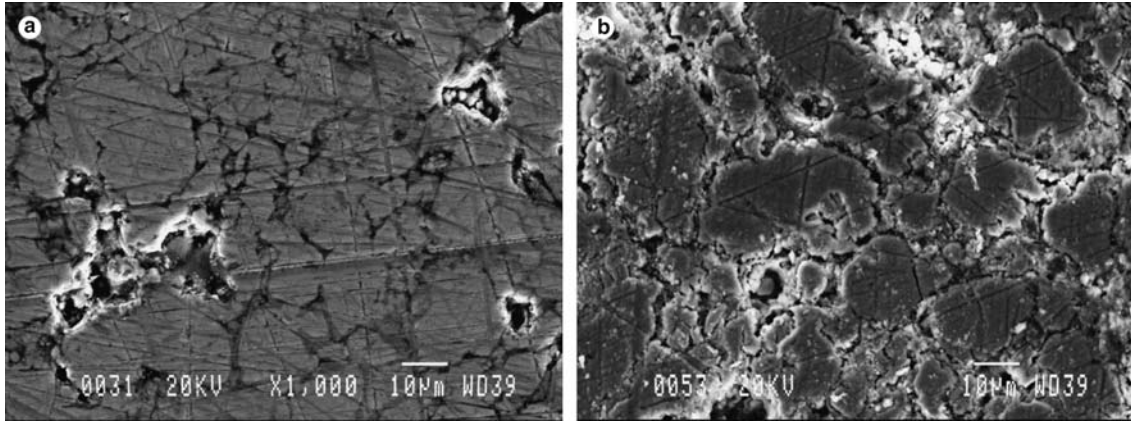


Fig. 6. Scanning electron micrographs of the  $\text{Ni}_2\text{Al}_5\text{Mo}_{0.175}$  electrode: (a) before leaching; (b) after leaching aluminum in 25% KOH + 10% Na-K tartrate solution at 70 °C for 24 h.

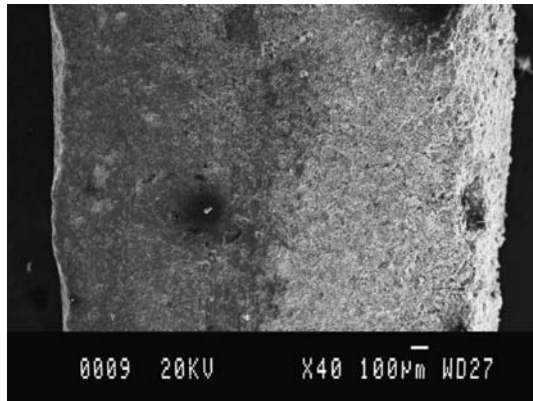


Fig. 7. Crosssection of the  $\text{Ni}_2\text{Al}_5\text{Mo}_{0.175}$  electrode after leaching; leaching was carried out from the right side of the electrode.

electrodes parameter  $\phi$  is lower than 1 (the lowest value is 0.85) this comparison is only approximate but it shows the general trend. These results suggest that the main factor of high activities of Raney Ni based

electrodes is the increase of the real surface area, while the intrinsic activity is lower or similar to that of polycrystalline Ni. Low activities of some electrodes may be connected with a presence of unleached Al in the pores, probably in the form of insoluble oxide/hydroxide, which could inhibit HER while allowing wetting of the pore surface (important in determination of  $C_{dl}$ ). The presence of Mo must also affect the electrode structure allowing better removal of Al and/or greater accessibility of the pores.

In our earlier studies it was found that various porous nickel based electrodes as Ni-Zn alloys [6], Raney Ni based materials [12, 13], pressed Ni-Zn and Ni-Al powder electrodes [12, 34, 35] have the intrinsic activity not much different from that of polycrystalline nickel [2, 36]. It was suggested in the literature that alloying Ni and Mo should increase the activity towards the HER, however, in many studies, the electrode surface was either covered with oxides/hydroxides or rough. Metallurgically obtained alloys are not very active. For more discussion and references see Ref. [1].

Table 2. Kinetic parameters of the HER from the steady-state polarization curves obtained in 1 M KOH

	Electrode	$t$ /°C	$b$ /mV dec <sup>-1</sup>	$\eta_{250}$ /mV	$j_0$ /mA cm <sup>-2</sup>
1	$\text{Ni}_2\text{Al}_3$	25	200	-280	5
2	$\text{Ni}_2\text{Al}_5$	25	157	-253	5
		70	173	-139	29
3	$\text{NiAl}_3$	25	99	-136	10.5
4	$\text{Ni}_2\text{Al}_3\text{Mo}_{0.175}$	25	180	-160	15
5	$\text{Ni}_2\text{Al}_5\text{Mo}_{0.175}$	25	170	-71	119
		70	120	-40	166
6	$\text{NiAl}_3\text{Mo}_{0.0875}$	25	156	-73	85
7	$\text{Ni}_2\text{Al}_3\text{Mo}_{0.233}$	25	170	-160	31
8	$\text{Ni}_2\text{Al}_5\text{Mo}_{0.233}$	25	154	-60	110
9	$\text{NiAl}_3\text{Mo}_{0.116}$	25	144	-58	110
10	$\text{Ni}_2\text{Al}_3\text{Mo}_{0.306}$	25	150	-70	97
11	$\text{Ni}_2\text{Al}_5\text{Mo}_{0.306}$	25	119	-66	96
		70	70	-43	39
12	$\text{NiAl}_3\text{Mo}_{0.153}$	25	134	-57	111
		70	80	-33	121
13	$\text{NiAl}_3\text{Mo}_{0.262}$	25	99	-60	71

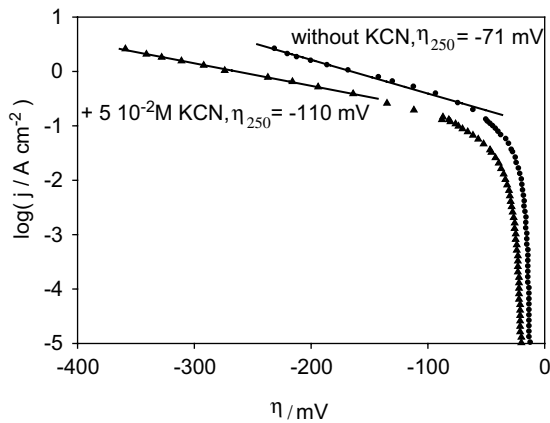


Fig. 8. Tafel plots obtained on  $\text{Ni}_2\text{Al}_5\text{Mo}_{0.175}$  electrode in 1 M KOH at 25 °C and after adding  $5 \times 10^{-2}$  M KCN.

#### 4.2. Plasma sprayed Ni–Al–Mo electrodes

##### 4.2.1. Composition and structure

Several materials of different composition were prepared. Electrode B was obtained from the mixture of

two pure binary phases  $\text{NiAl}_3$  (46%) and  $\text{Ni}_2\text{Al}_3$  (54%). XRD spectra show the presence of these two phases. Other electrode materials were prepared from a mixture of B with other ternary alloys (G, H I, T). The electrode T contains ternary phase  $\text{NiAl}_5\text{Mo}_2$ . It has been suggested in the literature [18, 37, 38] that this phase is responsible for the high activity of plasma sprayed NiAlMo electrodes towards water electrolysis. Figure 14 shows the diffractogram of this alloy. It contains strong peaks corresponding to this phase together with those corresponding to  $\text{Ni}_2\text{Al}_3$ . Leaching caused destruction of the electrode T, however other mixed phases were stable.

##### 4.2.2. Steady-state polarization curves

Tafel curves registered on plasma sprayed electrodes displayed one Tafel slope. The results are presented in Table 3. The obtained slopes are in the range 107–180  $\text{mV dec}^{-1}$ . The presence of molybdenum in the alloys increases the electrode activities, similarly to the results obtained above for the alloyed powders. The least active electrode B consists of Ni and Al, with  $\eta_{250} = -170$  mV while the most active material is

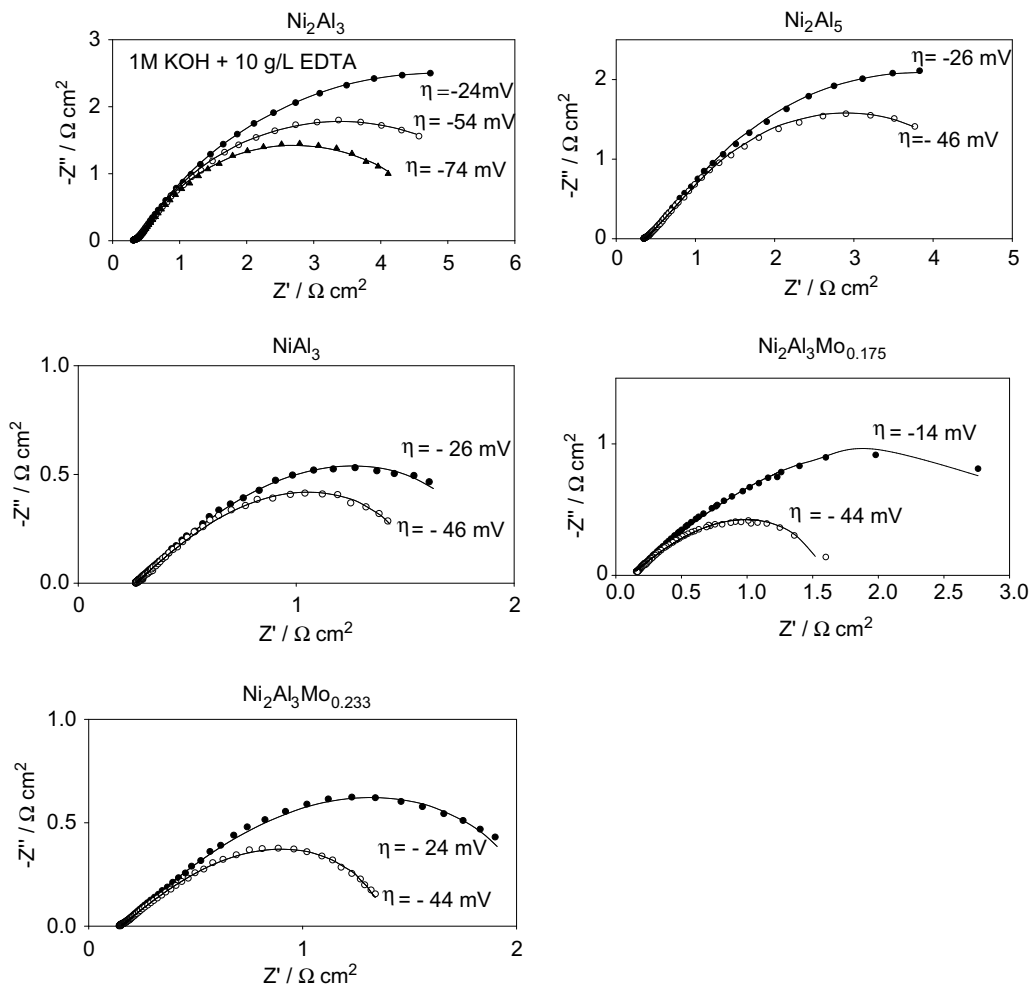


Fig. 9. Complex plane plots of the HER on Ni–Al and selected Ni–Al–Mo electrodes displaying one deformed semicircle, obtained in 1 M KOH at 25 °C; symbols – experimental data, continuous lines – fitted by the semi-infinite porous model (1CPE).

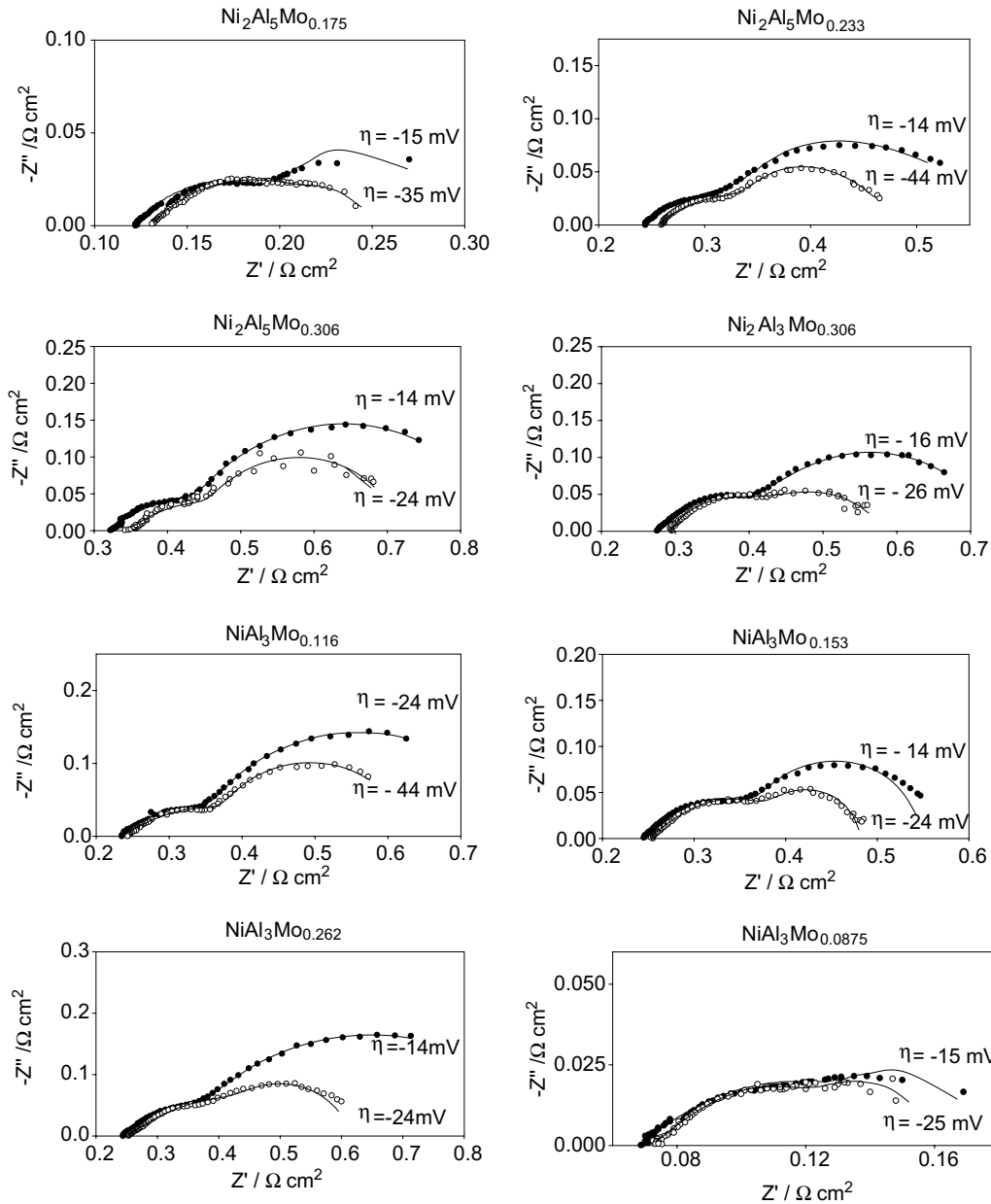


Fig. 10. Complex plane plots of the HER on Ni–Al–Mo electrodes displaying two semicircles, obtained in 1 M KOH at 25 °C; symbols – experimental data, continuous lines – fitted to the semi-infinite porous model (1CPE).

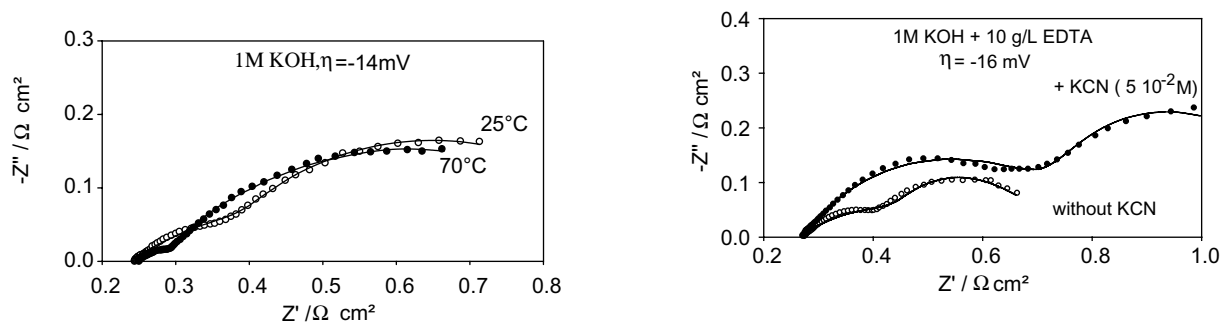


Fig. 11. Complex plane plots obtained in 1 M KOH at 25 °C and 70 °C at NiAl<sub>3</sub>Mo<sub>0.262</sub> electrode, points – experimental data, continuous lines – fitted to the semi-infinite porous model (1CPE).

Fig. 12. Complex plane plots obtained for Ni<sub>2</sub>Al<sub>3</sub>Mo<sub>0.306</sub> electrode in 1 M KOH at 25 °C without KCN and with  $5 \times 10^{-2}$  M KCN, points – experimental data, continuous lines – data fitted to the semi-infinite porous model (1CPE).

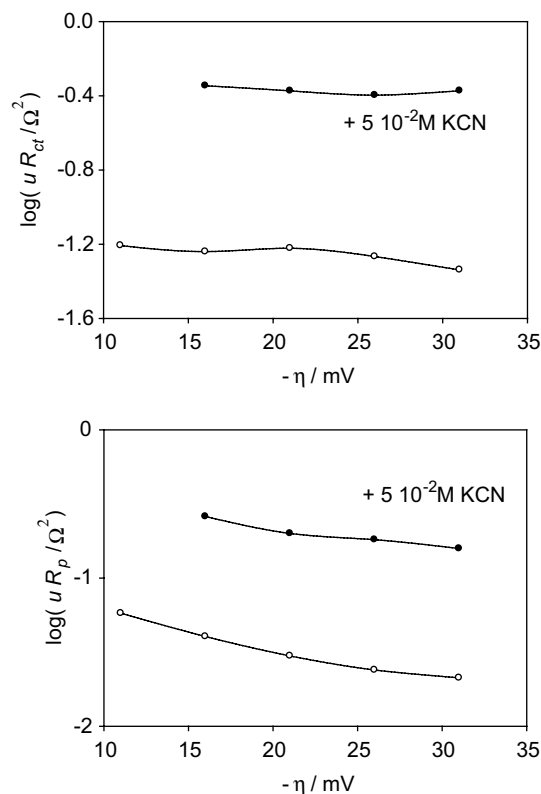


Fig. 13. Dependence of: (a) diameter of HF semicircle, (b) diameter of LF semicircle, on overpotential  $\eta$  for  $\text{Ni}_2\text{Al}_3\text{Mo}_{0.306}$  electrode in 1 M KOH without KCN and with  $5 \times 10^{-2}$  M KCN at 25 °C, semi-infinite porous model (ICPE).

$\text{NiAl}_{5.95}\text{Mo}_{0.66}$ , with  $\eta_{250} = -67$  mV. Further increase in the amount of Mo for the same composition Ni:Al (electrodes 22 and 23) does not improve the electrode activity. With exception of electrode G all other materials have similar activity,  $\eta_{250}$  between  $-100$  and  $-80$  mV.

#### 4.2.3. Impedance spectroscopy

Examples of the complex plane plots obtained on plasma sprayed electrodes are shown in Figure 15. For the mixture of binary phases (electrode B), a straight line at  $45^\circ$  at high frequencies followed by a

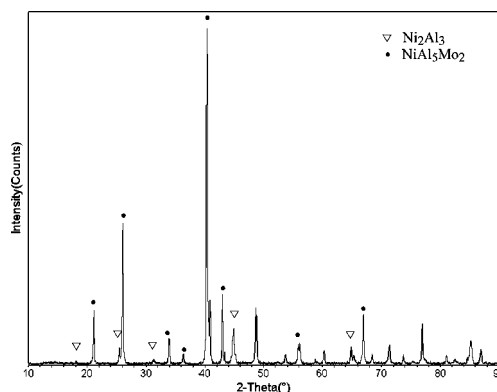


Fig. 14. XRD spectrum of plasma sprayed  $\text{NiAl}_5\text{Mo}_2$ .

semicircle was found, indicating finite-length porous model (compare with Figure 2(a)). For the other electrodes, two semicircles were obtained on the complex plane plots and the HF semicircle starts as a straight line at  $\sim 45^\circ$ . To determine the nature of the HF semicircle experiments were performed with addition of  $5 \times 10^{-2}$  M KCN and it was found that the diameter of two semicircles increased significantly. Therefore, the two semicircles are related to the electrode kinetics. To approximate these plots, semi-infinite porous model with the faradaic impedance described by Equation 6 was used. This is the same model that was used for heated powders containing Mo. Table 5 shows the results of the approximations of the impedance data. Parameter  $\phi$  is between 0.8 and 0.86, only for the electrode no. 19 it is lower,  $\phi = 0.7$ . The highest intrinsic activity shows electrode  $\text{NiAl}_{5.95}\text{Mo}_{0.66}$  followed by  $\text{NiAl}_{3.96}\text{Mo}_{1.32}$ . They display activities similar to that of Ni (taking into account values of  $\phi$  lower than 1 the differences are not significant) and other materials have lower intrinsic activities.

## 5. Conclusions

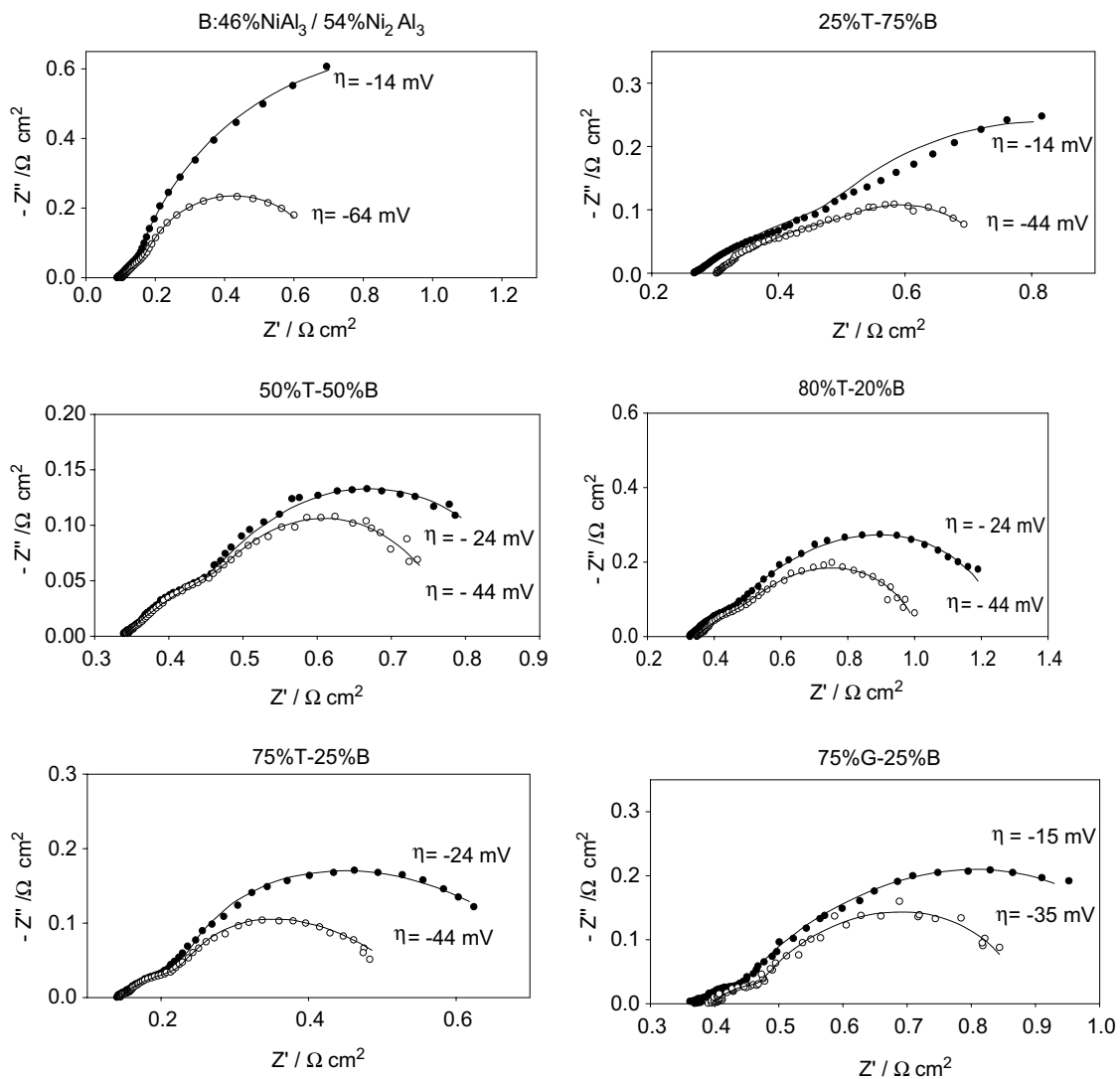
Raney nickel based electrodes are stable and very active towards the hydrogen evolution in alkaline solutions.

Table 3. Parameters obtained from the semi-infinite porous model (ICPE) at  $\eta = -35$  mV in 1 M KOH at 25 °C

Electrode	$uR_{ct}/\Omega^2$	$T/u/\text{F}\Omega^{-1} \text{ s}^{\phi-1}$	$\phi$	$1/(R_{ct}T)/\text{s}^{\phi-2}$
$\text{Ni}_2\text{Al}_3$	$74 \pm 1$	$2.5 \pm 0.1$	$1.00 \pm 0.01$	0.0054
$\text{Ni}_2\text{Al}_3\text{Mo}_{0.175}$	$1.5 \pm 0.1$	$2.0 \pm 0.1$	$0.88 \pm 0.02$	0.33
$\text{Ni}_2\text{Al}_3\text{Mo}_{0.233}$	$3.36 \pm 0.08$	$1.75 \pm 0.04$	$0.85 \pm 0.01$	0.17
$\text{Ni}_2\text{Al}_3\text{Mo}_{0.306}$	$0.046 \pm 0.004$	$15.66 \pm 0.52$	$0.89 \pm 0.02$	1.4
$\text{Ni}_2\text{Al}_5$	$40.0 \pm 0.3$	$5.2 \pm 0.1$	$1.00 \pm 0.01$	0.0048
$\text{Ni}_2\text{Al}_5\text{Mo}_{0.175}$	$0.098 \pm 0.008$	$12.17 \pm 0.80$	$1.00 \pm 0.01$	0.84
$\text{Ni}_2\text{Al}_5\text{Mo}_{0.233}$	$0.021 \pm 0.001$	$49 \pm 2$	$0.81 \pm 0.02$	0.97
$\text{Ni}_2\text{Al}_5\text{Mo}_{0.306}$	$0.027 \pm 0.002$	$24.67 \pm 2.15$	$0.95 \pm 0.03$	1.5
$\text{NiAl}_3$	$5.1 \pm 0.1$	$11.5 \pm 0.2$	$1.00 \pm 0.01$	0.017
$\text{NiAl}_3\text{Mo}_{0.0875}$	$0.2 \pm 0.01$	$11.04 \pm 0.40$	$0.90 \pm 0.01$	0.45
$\text{NiAl}_3\text{Mo}_{0.116}$	$0.07 \pm 0.01$	$28 \pm 1$	$0.81 \pm 0.02$	0.51
$\text{NiAl}_3\text{Mo}_{0.153}$	$0.033 \pm 0.002$	$17.76 \pm 0.82$	$0.95 \pm 0.03$	1.7
$\text{NiAl}_3\text{Mo}_{0.262}$	$0.06 \pm 0.004$	$18.3 \pm 0.50$	$0.82 \pm 0.01$	0.91

Table 4. Kinetic parameters of the HER from steady-state polarization curves obtained on plasma sprayed Ni–Al–Mo electrodes in 1 M KOH

	Electrode	$t$ /°C	$b$ /mV/dec	$\eta_{250}$ /mV	$j_0$ /mA cm <sup>-2</sup>
14	B = 46%NiAl <sub>3</sub> –54%Ni <sub>2</sub> Al <sub>3</sub> = NiAl <sub>1.95</sub>	25	143	-170	17
15	G: NiAl <sub>8</sub> Mo	25	173	-115	56
16	H: NiAl <sub>7.5</sub> Mo <sub>1.5</sub>	25	125	-88	55
17	I: NiAl <sub>5</sub> Mo <sub>0.67</sub>	25	104	-88	39
18	25%T–75%B = NiAl <sub>2.5</sub> Mo <sub>0.36</sub>	25	180	-100	62
19	50%T–50%B = NiAl <sub>3.15</sub> Mo <sub>0.79</sub>	25	173	-80	109
20	75%T–25%B = NiAl <sub>3.96</sub> Mo <sub>1.32</sub>	25	140	-85	89
21	80%T–20%B = NiAl <sub>4.15</sub> Mo <sub>1.44</sub>	25	140	-90	60
22	75%G–25%B = NiAl <sub>5.95</sub> Mo <sub>0.66</sub>	25	136	-67	274
23	75%H–25%B = NiAl <sub>5.62</sub> Mo <sub>0.99</sub>	25	107	-81	58

T: NiAl<sub>5</sub>Mo<sub>2</sub>.Fig. 15. Complex plane plots obtained in 1M KOH at 25 °C for plasma sprayed electrodes (T = NiAl<sub>5</sub>Mo<sub>2</sub>, G = NiAl<sub>8</sub>Mo), symbols – experimental data, continuous lines – fitted by the semi-infinite porous model (ICPE).

After leaching in alkaline solution some of Al was always present in the electrode material. It has been suggested in the literature [39] that 5–6 wt.% of Al should be left in the electrodes to maintain high

electrocatalytic activity. The electrode activity increases with increase in Al (porosity effect). Addition of Mo increases significantly the apparent electrode activity, although beyond a certain amount (0.233/NiAl) no

Table 5. Parameters obtained on plasma sprayed electrodes from the semi-infinite porous model (1CPE) at  $\eta = -35$  mV in 1 M KOH at 25 °C

Electrode	$uR_{ct}$ / $\Omega^2$	$T/u$ / $F\Omega^{-1} s^{\phi-1}$	$\phi$	$1/(R_{ct}T)$ / $s^{-1}$
NiAl <sub>2.5</sub> Mo <sub>0.36</sub>	0.196 ± 0.013	29.6 ± 0.4	0.8 ± 0.01	0.17
NiAl <sub>3.15</sub> Mo <sub>0.79</sub>	0.17 ± 0.01	18.4 ± 0.5	0.7 ± 0.01	0.32
NiAl <sub>3.96</sub> Mo <sub>1.32</sub>	0.023 ± 0.001	27.8 ± 0.6	0.83 ± 0.01	1.56
NiAl <sub>4.15</sub> Mo <sub>1.44</sub>	0.151 ± 0.015	10.72 ± 0.31	0.86 ± 0.01	0.62
NiAl <sub>5.95</sub> Mo <sub>0.66</sub>	0.025 ± 0.002	14.3 ± 0.9	0.86 ± 0.01	2.8

further improvement or even decrease in activity is observed.

Our electrodes prepared by interdiffusion of Al into Ni are more active than those obtained by direct alloying [15]. Raney Ni electrodes (50/50 wt.%, corresponding to NiAl<sub>2.17</sub>) prepared by sintering of Raney Ni at 1400 °C at high pressure [14] or sintering at 1600 °C [13] display a little higher activity than the electrodes studied in this work.

Plasma sprayed materials are more active than those prepared by heating Ni and Al powders having similar composition. Ternary phase, NiAl<sub>5</sub>Mo<sub>2</sub>, which was suggested to be responsible for high activity [18, 37, 38], is not stable and disintegrates during leaching. However, electrodes prepared with addition of this phase are stable and active.

Electrochemical impedance studies revealed that the semi-infinite porous model describes the behavior of the thermally synthesized materials while finite-length describes those prepared by plasma spraying. This indicates a different porous structure of the materials. One semicircle was observed for electrodes containing little or no Mo and lower Al content while for other materials two semicircles were observed. Both semicircles were of kinetic origin. Plasma sprayed NiAlMo electrodes (prepared by DLR) [10] displayed two semicircles but the first, very small one, was attributed to electrode porosity. This shows that the structure and porosity of these electrodes was different.

The intrinsic activity, expressed as the parameter  $1/(uR_{ct})(C_{dl}/u) = 1/(R_{ct}^0 C_{dl}^0)$  per unit of the real surface area is proportional to the inverse of the harmonic rate constant average of the Volmer and Herovskiy reactions,  $1/k = 1/k_1 + 1/k_2$ . Although the comparison of intrinsic activities was performed at  $\eta = -35$  mV, at which terms containing  $\exp(f\eta)$  in Equation 10 cannot be completely neglected, the general trend is evident. All the NiAl based electrodes have intrinsic activities much lower than that estimated for polycrystalline Ni. Addition of Mo and Al increases the activity but the highest activity is similar to that of polycrystalline Ni. This indicates that the main factor influencing the electrode activity is the increase in real surface area, although some catalytic effect of Mo cannot be excluded for one of the electrodes. The presence of Mo must affect the electrode structure and increase the accessibility of pores to the HER. The electrodes are good candidates for industrial water electrolysis.

## Acknowledgments

Mr. Glen Lemoine and Prof. Jerzy Jurewicz from CRTP, Université de Sherbrooke, are gratefully acknowledged for preparing the electrode materials by vacuum plasma spraying. Financial support from FQRNT (Québec), CRSNG and Université de Sherbrooke is also acknowledged.

## References

1. A. Lasia, 'Fuel Cell Electrocatalysis' in W. Vielstich, A. Lamm and H.A. Gasteiger (eds.), 'Handbook of Fuel Cell Technology' Vol. 2, (John Wiley & Sons Ltd., 2003), p. 416.
2. A. Lasia, *Current Top. Electrochem.*, **2** (1993) 239.
3. Y. Choquette, L. Brossard, A. Lasia and H. Ménard, *J. Electrochem. Soc.* **137** (1990) 1723.
4. Y. Choquette, L. Brossard, A. Lasia and Ménard, *Electrochim. Acta* **35** (1990) 1251.
5. Y. Choquette, H. Ménard and L. Brossard, *Int. J. Hydrogen Energy* **15** (1990) 1.
6. L. Chen and A. Lasia, *J. Electrochem. Soc.* **138** (1991) 3321.
7. D.E. Hall, *J. Appl. Electrochem.* **14** (1984) 107.
8. G.K. Lohrberg and P. Kohl, *Electrochim. Acta* **29** (1984) 1557.
9. G. Schiller and V. Borck, *Int. J. Hydrogen Energy* **17** (1992) 261.
10. D. Miousse, A. Lasia and V. Borck, *J. Appl. Electrochem.* **25** (1995) 592.
11. H. Wendt, H. Hoffman and V. Plazak, *Mater. Chem. Phys.* **22** (1989) 27.
12. L. Chen and A. Lasia, *J. Electrochem. Soc.* **140** (1993) 2464.
13. P. Los, A. Rami and A. Lasia, *J. Appl. Electrochem.* **23** (1993) 135.
14. A. Rami and A. Lasia, *J. Appl. Electrochem.* **22** (1992) 376.
15. S. Tanaka, N. Hirose, T. Tanaki and Y.H. Ogata, *J. Electrochem. Soc.* **147** (2000) 2242.
16. H. Ewe, E. Justi and A. Schmitt, *Electrochim. Acta* **19** (1974) 799.
17. J. Divisek, H. Schmitz and J. Balej, *J. Appl. Electrochem.* **19** (1989) 519.
18. G. Schiller, R. Henne and V. Borck, *J. Thermal Spray Technol.* **4** (1995) 185.
19. A. Lasia and A. Rami, *J. Electroanal. Chem.* **294** (1990) 123.
20. D.A. Harrington and B.E. Conway, *Electrochim. Acta* **32** (1987) 1703.
21. A. Lasia, in B.E. Conway and R.E. White (eds.), 'Modern Aspects of Electrochemistry' Vol. 35 (Kluwer/Plenum, New York, 2002), p. 1.
22. A. Lasia, in G. Jerkiewicz and P. Marcus (eds.), 'Proceeding of the Electrochemical Society Symposium on Electrochemical Surface Science of Hydrogen Adsorption and Absorption' Vol. 97-16 (The Electrochemical Society, 1997), p. 27.
23. G.J. Brug, A.L.G. Van der Eeden, M. Sluyters-Rehbach and J. Sluyters, *J. Electroanal. Chem.* **176** (1984) 275.
24. T. Pajkossy, *J. Electroanal. Chem.* **364** (1994) 111.
25. Z. Kerner and T. Pajkossy, *Electrochim. Acta* **46** (2000) 207.
26. T. Pajkossy, T. Wandlowski and D.M. Kolb, *J. Electroanal. Chem.* **414** (1966) 209.
27. A. Lasia, *Int. J. Hydrogen Energy* **18** (1993) 557.

28. L. Chen and A. Lasia, *J. Electrochem. Soc.* **139** (1992) 3214.
29. R. De Levie, in P. Delahay and C.W. Tobias (eds.), 'Advances in Electrochemistry and Electrochemical Engineering' Vol. 6 (Wiley, 1967), p. 239.
30. P. Los, A. Lasia and H. Ménard, *J. Electroanal. Chem.* **360** (1993) 101.
31. C. Hitz and A. Lasia, *J. Electroanal. Chem.* **500** (2000) 213.
32. J.R. Macdonald, J. Schoonman and A. P. Lehner, *J. Electroanal. Chem.* **131** (1982) 77.
33. D.E. Brown, M.N. Mahmood, M.C.M. Man and A.K. Turner, *Electrochim. Acta* **29** (1984) 1551.
34. L. Chen and A. Lasia, *J. Electroanal. Soc.* **139** (1992) 3214.
35. C. Hitz and A. Lasia, *J. Electroanal. Chem.* **532** (2002)133.
36. A. Lasia, in B.E. Conway and G. Jerkiewicz (eds.), 'Proceedings of the Symposium on Electrochemistry and Materials Science of Cathodic Hydrogen Absorption and Adsorption' Vol. 94-21 (The Electrochemical Society, 1995), p. 261.
37. A. Kayser, V. Borck, M. von Bradke, R. Henne, W.A. Kaysser and G. Schiller, *Z. Metallkd.* **83** (1992) 565.
38. F. Berubé, M.Sc. *Thesis*, Université de Sherbrooke (1996).
39. S. Tanaka, N. Hirose and T. Tanaki, *Denki Kagaku* **12** (1997) 1044.